Collisionless Coupling in the AMPTE Artificial Comet

K. Papadopoulos

Science Applications International Corporation, McLean, Virginia

J. D. Huba

*Geophysical and Plasma Dynamics Branch, Plasma Physics Division
Naval Research Laboratory, Washington, D. C.*

A. T. Y. Lui

Applied Physics Laboratory, Johns Hopkins University, Laurel, Maryland

Analysis of previously reported observations of the solar wind–barium interaction associated with the AMPTE artificial comet release of December 27, 1984, is presented. On the basis of these results we argue that the solar wind couples momentum (and energy) to the barium ions through both laminar and turbulent processes. The laminar forces acting on the particles are the laminar electric and magnetic fields; the turbulent forces are associated with the intense electrostatic wave activity. This wave activity is shown to be caused by a cross-field solar wind proton–barium ion streaming instability. The observed wave frequencies and saturated amplitudes are consistent with our theoretical analysis.

1. Introduction

The in situ measurements of the plasma parameters from the AMPTE (Active Magnetospheric Particle Tracer Explorers) artificial comet releases [*Valenzuela et al.*, 1986; *Haerendel et al.*, 1986] in the solar wind provide us with a unique set of data to test the available theories on the subject of collisionless coupling of magnetized plasma streams under high Mach number conditions ($M_A \gg 1$) [*Haerendel et al.*, 1986]. The subject is very opportune since it is the controlling factor that determines the momentum coupling process occurring in the interaction of the solar wind with the cometary plasma generated by the ionization of the neutral coma. The overall comet structure, the applicability of MHD or kinetic models, the presence or absence of a cometary shock, and the type of the resulting ionopause [*Mendis and Houpis*, 1982; *Ip and Axford*, 1982; *Fedder et al.*, 1986; *Sagdeev et al.*, 1986] depend critically on the wave-particle processes producing the momentum coupling, the thermalization, and the isotropization in the interaction. It is the purpose of the present note to compare the AMPTE in situ observations of the plasma parameters and wave signatures [*Gurnett et al.*, 1985; *Haerendel et al.*, 1986] with the theoretical concepts currently applied to the high Mach number interaction problem. In the next section we present a brief description of the experiment as well as the relevant data. Section 3 reviews the theoretical models for coupling. Section 4 compares the AMPTE data with the observations.

2. Observational Results

During the artificial comet experiment on December 27, 1984, two canisters of barium were released from the IRM (Ion Release Module) spacecraft. The release was on the

morning side of the earth at a geocentric radial distance of roughly 17 earth radii. The canisters were exploded simultaneously at a distance ~ 1 km from the spacecraft at 1232 UT. The explosion produced an expanding barium cloud which was rapidly ionized by solar UV ($\tau_i \simeq 28$ s where τ_i is the photoionization time). The interaction of the solar wind, which was flowing at ~ 550 km/s, with the ionized barium cloud was recorded by the IRM instruments inside the cloud and the magnetic cavity that was created. The UKS spacecraft, located ~ 170 km away, was outside the magnetic cavity and measured magnetic disturbances and particle fluxes generated by the interaction. A schematic of the spacecraft positions and the magnetic field structure is shown in Figure 1. We comment that in addition to the in situ observations made by the IRM and UKS spacecraft, ground-based and airborne optical data were also obtained during the release. Such data provide important information on the macroscopic behavior of the solar wind–barium interaction. However, for the purposes of the present study, these data are not used since we are concerned with the detailed evolution of plasma and field quantities which is not provided by optical data.

In Figures 2–4 we present a set of plasma and field measurements which highlight the dynamic interaction of the solar wind and the barium cloud. In Figure 2 we show measurements of the electron density from 15 eV to 30 eV (n_e (Figure 2a)), the flow velocity of the solar wind protons measured in the range 20 eV to 40 keV in GSE coordinates (V_{px} (Figure 2b) and V_{pz} (Figure 2c)), and the magnitude of the interplanetary magnetic field (B (Figure 2d)) [*Haerendel et al.*, 1986]. We note that the magnetic field is in the y direction and that the electron density does not include the cold electrons associated with the barium ions. The magnetic cavity generated by the barium ions is clearly seen during the time 1232:02–1233:15 UT. Figure 3 shows the low-frequency electric field measurements as a function of time and frequency [*Gurnett et al.*, 1985], the magnitude of the magnetic field, and the barium ion density. Figure 4 displays the electric field spectrum upstream of the ion cloud at the time of maximum intensity (1234:27
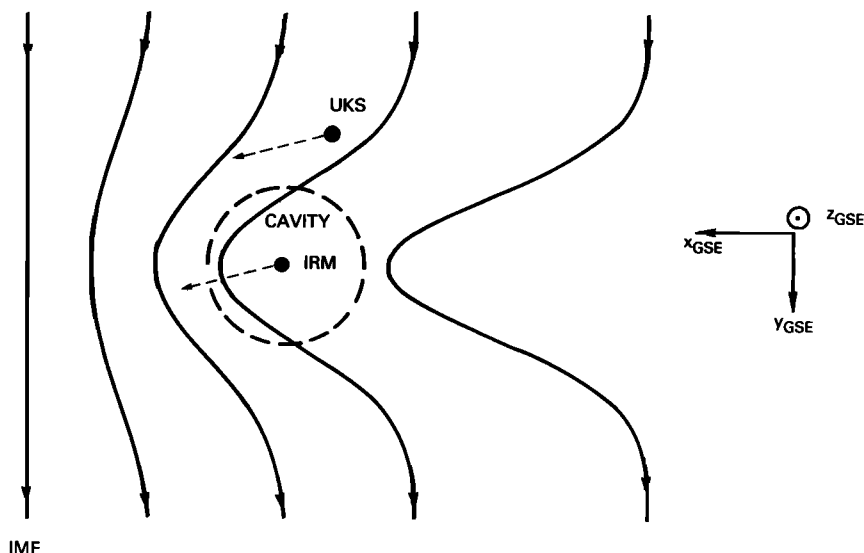
Fig. 1.   Schematic of the spacecraft positions and magnetic field structure for the December 27, 1984, AMPTE release.   ·

UT) [*Gurnett et al.*, 1985]. The electrostatic waves reached amplitudes in excess of 140 mV/m. Since the electron density in Figure 2 does not include the cold electrons, for times prior to 1234:30 UT we will use the number density from Figure 3, which is based upon wave emissions at the plasma frequency. For the time period 1234:30–1235:30 UT the values of the electron, proton, and barium densities are not well known. Finally, for times later than 1235:30 UT we use the data presented in Figure 2.

On the basis of these measurements the following picture describing the spatial evolution of the coupling between the solar wind protons and the barium emerges. For times later than 1236:20 UT the solar wind parameters correspond to the ambient conditions ($n_e \approx 2$ cm^{-3}, $V_{px} \approx 550$ km/s, $T_e \approx 2 \times 10^5$ °K, and $B \approx 10 \gamma$). The interaction between the solar wind protons and the barium cloud starts at the point marked
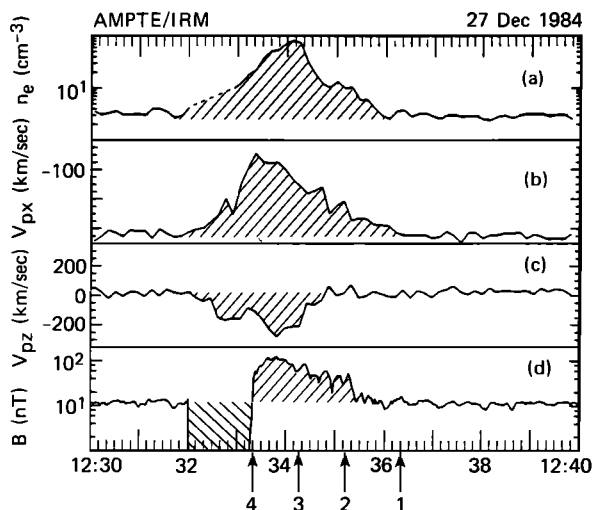

Fig. 2.   Particle and field data [from *Haerendel et al.*, 1986]. (*a*) Electron density (cm^{-3}). (*b*) Solar wind proton velocity (kilometers per second) in the x direction (GSE coordinates). (*c*) Solar wind proton velocity (kilometers per second) in the z direction (GSE coordinates). (*d*) Magnetic field (nanoteslas).
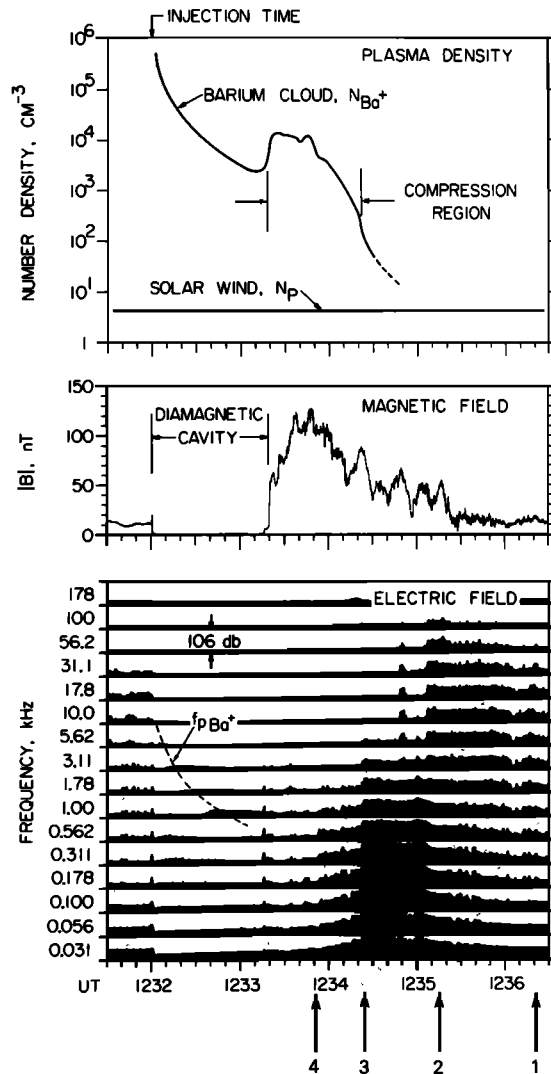

Fig. 3.   Particle, field, and electric field wave data [from *Gurnett et al.*, 1985]. The barium ion density is based upon emissions at the plasma frequency. Note the intense, low-frequency ($f \sim 30$ Hz to 1 kHz) electrostatic waves between the times marked 2 and 3.

1, which corresponds to 1236:20 UT, as seen from the initiation of the slowing down of the solar wind (Figure 2b). During the time period 1236:20–1235:15 UT the initial slowing down rate is relatively weak and is accompanied by moderate wave activity (Figure 3), density, and magnetic field compression (Figures 2a and 2d). There is no plasma flow in the z direction (Figure 2c). This time coincides with the time that the UK spacecraft records fluxes of hot electrons (> 100 eV). A much stronger slowing down rate is observed between 1235:15 and 1234:25 UT, accompanied by strong electrostatic wave activity near the local proton lower hybrid frequency. For $B \simeq$ 30–90 γ, $n_p \simeq$ 2–10 cm^{-3}, and $n_e \simeq$ 2–120 cm^{-3} we note that the proton lower hybrid frequency is $f_{Hp} \simeq$ 10–30 Hz. The magnetic field, density, and temperature continue to increase, while the value of V_{pz} remains relatively unchanged. This continues until 1234:25 UT, which is marked as 3. At this point the magnetic field has a value $B = 85$ γ, and the solar wind stream has slowed down to $V_{px} \approx$ 270 km/s, corresponding to 0.4 keV flow energy, while a broad ion distribution is observed with an equivalent temperature of 4 × 10^6 °K (i.e., 0.4 keV). Notice that at this point the solar wind has lost more than 80% of its flow energy and its thermal spread is comparable to its flow speed. This corresponds to the peak of the electrostatic wave activity (see Figure 3). The slowing down of the solar wind continues until 1233:20 UT. The magnetic field exceeds 120 γ and approaches its maximum value of 145 γ. Finally, at 1233:15 we note the beginning of the magnetic cavity, the suppression of the wave activity, and the appearance of sunward flowing 0.5-keV ions. A summary of the key parameters observed during the above times is given in Table 1.
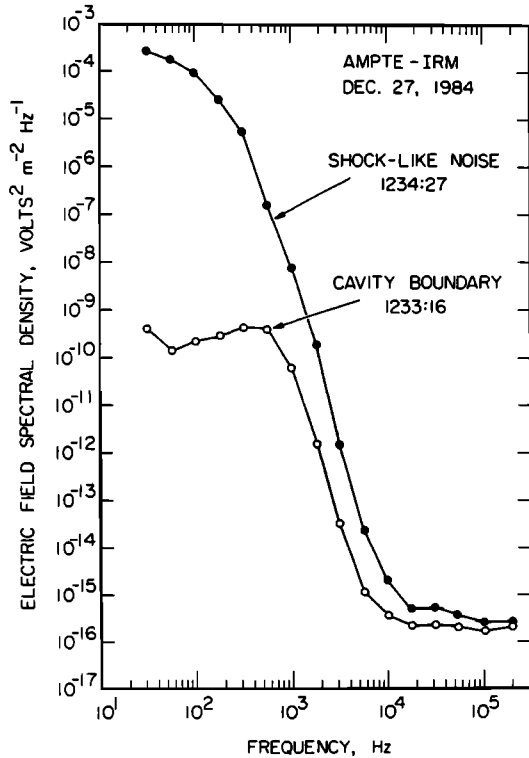

Fig. 4. Electric field spectral density as a function of frequency for times 1234:27 and 1233:16 UT [from *Gurnett et al.*, 1985]. Note that the most intense waves for 1234:27 UT (marked 3 in Figures 2 and 3) are low frequency (i.e., $f \sim$ 30 Hz).

TABLE 1. Plasma Parameters for the December 27, 1984, AMPTE Release

UT	V_{px}, km/s	V_{pz}, km/s	B, γ	n_e, cm^{-3}	n_p, cm^{-3}	n_{Ba}, cm^{-3}	f_{Hp}, Hz	V_{Ap}, km/s
1236:20	−550	0	20	6*	5	1*	12	195
1235:15	−400	0	50	20*	10*	10*	23	345*
1234:27	−250	−50	85	110	10*	100	17	586*
1233:50	−75	−250	130	3010	10*	3000	5	896*

*Estimate.

We note that there is a marked difference in the nature of the slowing down of the solar wind between the time periods 1236:20–1235:27 UT and 1235:27–1234:17 UT. In the former case we point out that the low-frequency electrostatic wave activity is intense and that there is little change in the z component of the solar wind velocity. In the latter time period, the electrostatic noise has weakened considerably, and there is a substantial increase in V_{pz}. These issues will be discussed in more detail in section 4.

3. COLLISIONLESS MOMENTUM COUPLING: THEORETICAL CONCEPTS

Prior to discussing the interpretation of the above data with respect to the physics of momentum coupling, we present a brief review of the various coupling processes. We consider the following momentum equation in the x direction for a solar wind proton (i.e., radial direction perpendicular to the ambient magnetic field $\mathbf{B} = B\hat{e}_y$).

$$\frac{dV_{px}}{dt} = \frac{eE_x}{m_p} + \Omega_p V_{pz} - v^*(V_{px} - V_b) \qquad (1)$$

where the subscript p refers to solar wind protons, $\Omega_p = eB/m_p c$, v^* is an anomalous ion-ion collision frequency, $V_b = V_b \hat{e}_x$ is the streaming barium velocity, e is the charge, and m is the mass. The first term on the right-hand side of (1) arises from a laminar electric field usually associated with the leading edge of the magnetic compression; it acts to accelerate barium ions and to slow down solar wind protons. The second term is the magnetic force which is associated with Larmor coupling. The final term corresponds to turbulent "pickup" of the solar wind and arises because of plasma instabilities. For plasma turbulence such that $v^* > \Omega_p$ it is clear that turbulent coupling can dominate over Larmor coupling. Also, notice that the force $\Omega_p V_{pz}$ associated with Larmor coupling is proportional to the value of V_{pz} and will be very weak as long as $V_{pz} \approx$ 0. The time evolution of V_{pz} is given by

$$\frac{dV_{pz}}{dt} = \frac{eE_z}{m_p} = \frac{eV_{px}B}{m_p c} = \Omega_p V_{px} \qquad (2)$$

In deriving (2) we assume $E_z = V_{px}B/c$, which is the motional electric field of the solar wind.

The subject of the appropriate value of v^* and the dominant instability that drives it has been extensively studied. We refer the interested reader to *Lampe et al.* [1975] and summarize only their key conclusions. The counterstreaming between the barium ions and solar wind protons generates a local velocity distribution function such as shown in Figure 5. Figure 5 is drawn for convenience in the solar wind reference frame. For singly ionized barium the electrons have a relative velocity
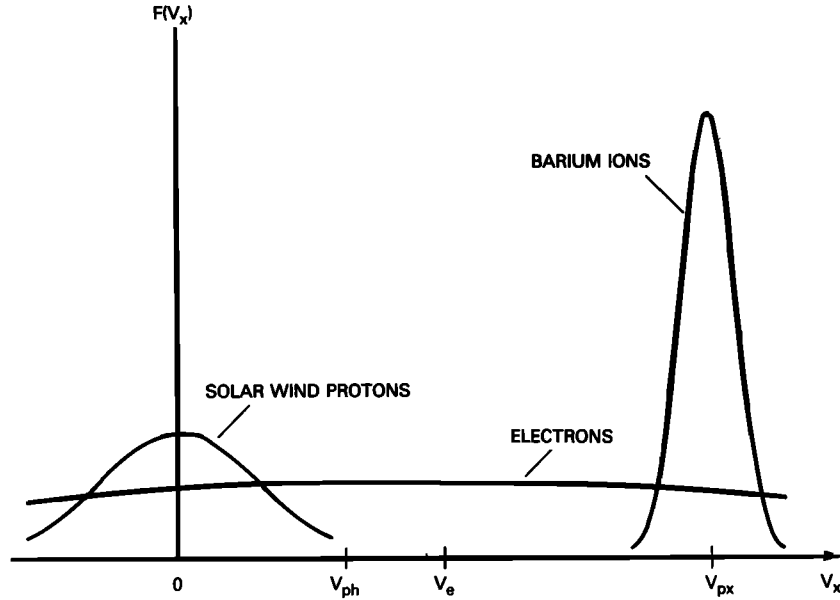
Fig. 5. Local velocity distributions of the solar wind protons, barium ions, and electrons in the solar wind frame of reference.

$\mathbf{V} = V_e \hat{e}_x$ with respect to the solar wind protons given by $V_e = V_{px}(n_b/n_e)$ where n_b is the density of the barium and $n_e = n_b + n_p$.

The dispersion equation for this situation is given by [Papadopoulos et al., 1971]

$$D(\omega, k) = \frac{\omega_b^2}{k^2 v_b^2} Z'\left(\frac{\omega - kV_{px}\cos\theta}{kv_b}\right) + \frac{\omega_p^2}{k^2 v_p^2} Z'\left(\frac{\omega}{kv_p}\right)$$
$$+ 1 + \frac{\omega_e^2}{\Omega_e^2}\left[1 + \frac{\omega_e^2}{c^2 k^2}(1 + \beta_e)^{-1}\right] = 0 \qquad (3)$$

where $\omega_\alpha = (4\pi n_\alpha e^2/m_\alpha)^{1/2}$ is the plasma frequency and $v_\alpha = (T_\alpha/m_\alpha)^{1/2}$ is the thermal speed of species α (e: electron; b: barium; p: proton),

$$\mathbf{k} = k_x \hat{e}_x + k_z \hat{e}_z \qquad \theta = \tan^{-1}(k_z/k_x) \qquad \mathbf{V}_p = V_{px}\hat{e}_x$$

$\Omega_e = eB/m_e c$ is the electron cyclotron frequency, $\beta_e = 8\pi n_e T_e/B^2$, and $Z'(\zeta) = -2[1 + \zeta Z(\zeta)]$ with Z the plasma dispersion function. In writing (3) we have assumed $\mathbf{k} \cdot \mathbf{B} = 0$ (i.e., $k_y = 0$) so that we are only considering flute modes, and have assumed that the ions are unmagnetized (valid for $\omega > \Omega_{p,b}$ and $k\rho_{p,b} \gg 1$ where $\rho_{p,b}$ is the mean ion Larmor radius of the protons and barium ions, respectively) and the electrons are magnetized. We comment that retaining a finite k_y can generate the modified two-stream instability [McBride et al., 1972]. However, this instability produces little momentum coupling between the counterstreaming ions; it primarily heats electrons and generates electron tails parallel to $\mathbf{B}$.

We can simplify (3) by assuming cold ions, i.e., $v_b \ll \omega/k - V_{px}\cos\theta$ and $v_p \ll \omega/k$. In this limit, $Z(\zeta) \simeq -1/\zeta - 1/2\zeta^3$, and (3) can be written as

$$\frac{\alpha\omega_{Hp}^2}{(\omega - \mathbf{k} \cdot \mathbf{V}_p)^2} + \frac{\omega_{Hp}^2}{\omega^2} = 1 + \frac{\omega_0^2}{k^2 c^2} \qquad (4)$$

where the proton lower hybrid frequency is

$$\omega_{Hp}^2 = \omega_p^2(1 + \omega_e^2/\Omega^2)^{-1} \qquad (5a)$$

$$\alpha = \frac{n_b}{n_p}\frac{m_p}{m_b} \qquad (5b)$$

$$\omega_0^2 = \frac{\omega_e^2}{\Omega_e^2}\frac{\omega_e^2}{(1 + \omega_e^2/\Omega_e^2)(1 + \beta_e)} \qquad (5c)$$

Notice that as long as $n_b/n_p < m_b/m_p \approx 137$ then $\alpha < 1$ and the small term in the dispersion relation is due to barium ions. This implies that when $n_b/n_p < 137$ the excited waves will be proton, rather than barium, lower hybrid waves.

For $\alpha < 1$ and $\omega_0^2 \ll c^2 k^2$, the most unstable waves have the following approximate frequency and wave number:

$$\omega_r \simeq \omega_{Hp} \qquad (6a)$$

$$\gamma \simeq 0.69\alpha^{1/3}\omega_{Hp} \qquad (6b)$$

$$k\cos\theta \simeq \omega_{Hp}/V_{px} \qquad (6c)$$

On the other hand, for values of $\omega_0^2/c^2 k^2$ sufficiently large, the modes can be stabilized because of electromagnetic effects [Papadopoulos et al., 1971; Lampe et al., 1975]. The criterion for instability is given by
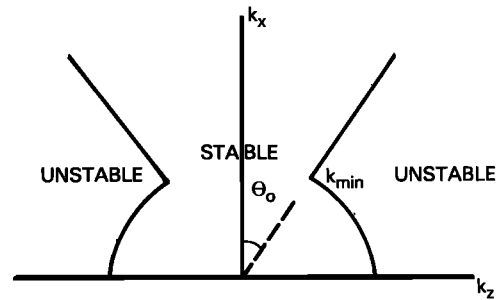

Fig. 6. Schematic of unstable waves driven by the magnetized ion-ion instability in the k_x-k_z plane. The relative drift between ions is in the x direction.
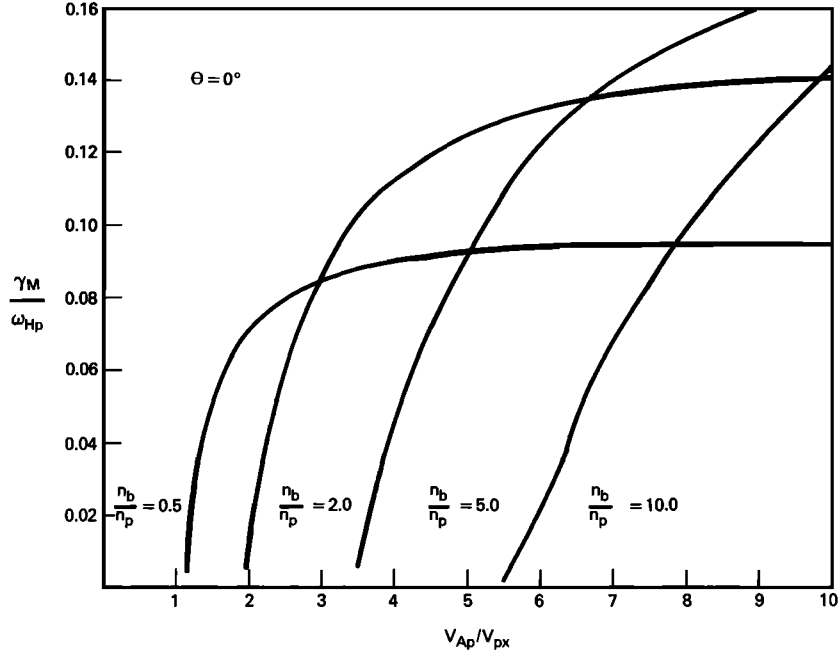
Fig. 7.   Plot of γ_M/ω_{Hp} versus V_{ap}/V_{px} for $\theta = 0°$ and $n_b/n_p = 0.5, 2.0, 5.0, 10.0$. Here γ_m is the maximum growth rate with respect to the wave number k.

$$\cos \theta < \frac{c\omega_{Hp}}{V_{px}\omega_e} (1 + \alpha^{1/3})^{3/2}(1 + \beta_e)^{1/2} = \cos \theta_0 \qquad (7)$$

For the parameters of interest, we note that $\alpha \ll 1$ and $\beta_e \ll 1$, so that (7) can be rewritten as

$$\cos \theta < \frac{V_{Ap}}{V_{px}}\left(1 + \frac{n_b}{n_p}\right)^{-1} \qquad (8)$$

where $V_{Ap} = B/(4\pi n_p m_p)^{1/2}$ is the local Alfvén velocity associated with the protons. Notice that the angle θ_0 separates the angular region of unstable modes from stable modes in the plane perpendicular to the magnetic field (Figure 6). For values of the right-hand side of (8) which are comparable to or larger than unity, the entire k space plane is unstable, and as shown by Lampe et al. [1975], complete ion-ion momentum coupling accompanies the interaction. The instability weakens substantially when the stable region around V_p increases (i.e., θ_0 increases), leaving only weak off-angle modes unstable.

To better illustrate the linear properties of the counterstreaming ion-ion instability, we present numerical solutions of (3) for parameters relevant to the AMPTE release of December 27, 1984. In Figures 7 and 8 we take $m_b/m_p = 137$, $v_p/V_{px} = 0.3$, $v_b/V_{px} = 0.01$, and $\beta_e = 0.0$. The most significant variations are for n_b/n_p and V_{Ap}/V_{px}, so we present results for a range of values for these parameters. In Figures 7 and 8 we plot γ_M/ω_{Hp} versus V_{Ap}/V_{px} for $n_b/n_p = 0.5, 2.0, 5.0$, and 10.0 (or $\alpha = 3.7 \times 10^{-3}, 1.5 \times 10^{-2}, 3.7 \times 10^{-2}$, and 7.4×10^{-2}, respectively). In Figure 7 we consider $\theta = 0°$, while in Figure 8 we consider $\theta = 60°$. Here γ_M is the maximum growth rate as a function of k. We have not plotted ω, or k but note that (6a) and (6c) are in reasonable agreement with the numerical values. In Figure 7 we note the following. First, in the limit $V_{Ap}/V_{px} \gg 1$, the growth rate asymptotes to its maximum value, which is approximately given by (6b) (e.g., for $n_b/n_p = 0.5$ ($\alpha = 3.7 \times 10^{-3}$) we obtain $\gamma_M/\omega_{Hp} \simeq 0.108$). Also, in this

limit we note that the maximum growth rate increases as n_b/n_p increases. Second, as V_{Ap}/V_{px} decreases, the growth rate decreases; for sufficiently small values of V_{Ap}/V_{px} the modes are stabilized because of electromagnetic effects. However, note that the critical value of V_{Ap}/V_{px} which stabilizes the modes decreases with decreasing n_b/n_p (e.g., for $V_{Ap}/V_{px} = 2$ the mode is stable for $n_b/n_p = 10.0$ but unstable for $n_b/n_p = 0.5$). This is consistent with (8), which, for $\theta = 0$, can be written as $V_{Ap}/V_{px} > (1 + n_b/n_p)$. We also note that the critical value of V_{Ap}/V_{px} predicted by (8) is somewhat greater than is found from Figure 7. That is, for $n_b/n_p = 0.5, 2.0, 5.0$, and 10.0, (8) predicts $\gamma = 0$ for $V_{Ap}/V_{px} = 1.5, 3.0, 6.0$, and 11.0, respectively; however, Figure 7 shows that $\gamma = 0.01\omega_{Hp}$ ($\simeq 0$) for $V_{Ap}/V_{px} = 1.2, 2.0, 3.6$, and 5.5. The reason for this is that (8) is based upon the assumption of cold protons ($\omega \gg kv_p$), but for the parameters used in Figure 7 (i.e., $v_p/V_{px} = 0.3$) this assumption breaks down as V_{Ap}/V_{px} decreases and thermal effects allow the modes to grow in the stable "cold" plasma regime.

In Figure 8 we plot γ_M/ω_{Hp} versus V_{Ap}/V_{px} for the same parameters as in Figure 7, but we consider $\theta = 60°$. The basic features of Figure 8 are the same as Figure 7. However, two points are worth mentioning. First, and most important, unstable modes exist for values of V_{Ap}/V_{px} that lead to stable modes in the case of $\theta = 0$. In fact, for all values of n_b/n_p considered, strong growth (i.e., $\gamma > 0.01\omega_{Hp}$) exists for $V_{Ap}/V_{px} > 2$, and in the case of $n_b/n_p = 0.5$ exists for $V_{Ap}/V_{px} > 0.5$. Again, this behavior is consistent with (8). Second, we note that for the same values of n_b/n_p the maximum growth rates are smaller for $\theta = 60°$ than $\theta = 0°$. This appears to be inconsistent with (6b), which indicates the maximum growth rate does not depend upon angle. The reason for the discrepancy is the effect of thermal protons which have a stabilizing influence because of ion Landau damping. Finally, we note that we have chosen $\theta = 60°$ because nonlinear studies have demon-
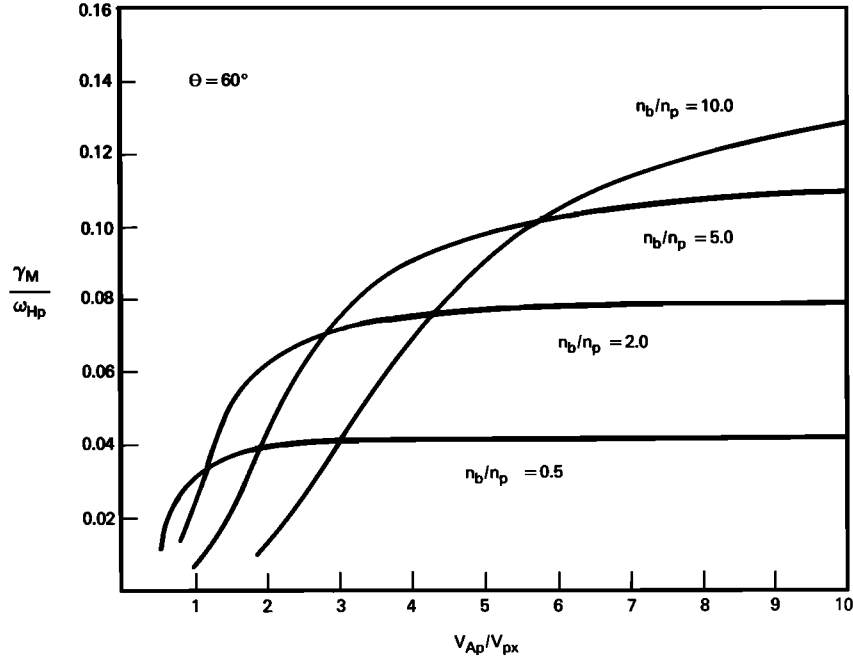
Fig. 8. Plot of γ_M/ω_{Hp} versus V_{Ap}/V_{px} for $\theta = 60°$ and $n_b/n_p = 0.5, 2.0, 5.0, 10.0$. Note that for these parameters ($\theta = 60°$) the modes are excited for lower values of V_{Ap}/V_{px} than in the previous case ($\theta = 0°$), consistent with (8).

strated that if the angular region of unstable waves initially satisfied the condition $\cos \theta < \cos \theta_0 \simeq 0.5$ (i.e., $\theta_0 = 60°$), then the entire k plane subsequently becomes unstable, resulting in complete momentum coupling between the ion streams. If $\cos \theta > 0.5$, then the situation, although mildly unstable, is quickly stabilized by finite temperature effects with little momentum coupling.

4. COMPARISON BETWEEN THEORY AND OBSERVATIONS

We now proceed to analyze the observations with the theoretical models described in section 3. Our approach is to examine in detail the key times marked as 1–4 in Figures 2 and 3. Table 1 gives the values of the important plasma parameters. We note that all of the data are not well known and we have made estimates of some values. Also, in comparing the theoretical conditions for instability with experimentally observed parameters, one does not expect to find "grossly" unstable conditions since the turbulence observed is generally in the nonlinear regime (i.e., near marginal stability).

The slowing down of the solar wind begins at the point marked 1 in Figures 2 and 3. From Table 1 we see that $n_b/n_p \simeq 0.2$ and $V_{Ap}/V_{px} \simeq 0.4$; from Figure 8, note that these conditions are marginally stable for the ion-ion instability. Therefore the beginning of the interaction is consistent with the minimum condition for a momentum coupling cross-field, counterstreaming proton-barium instability. The theoretically expected electrostatic waves cover the range between $f_{Hp} \approx 10$ Hz and $f_{ce} \approx 560$ Hz, with most of the energy confined in the 15- to 40-Hz region. At the time marked 2 (1235:15 UT) the magnetic field compression starts, and there is an attendant increase in V_{Ap}/V_{px}. Thus this leads to conditions more favorable to instability, and we expect the entire k plane to become unstable, leading to strong momentum coupling. Figures 2 and 3 seem to confirm this. The range of the unstable waves

corresponds to 22 Hz to 1.6 kHz with most of the energy in the 22- to 60-Hz region. Notice that between times marked 1 and 3, the value of V_{pz} is relatively unchanged and remains close to zero, while V_{px} is reduced sharply. The ion-ion driven interaction seems to terminate at the time marked 3 (1234:27 UT). At this time the solar wind speed is $|V_{px}| \approx 250$ km/s; the protons have lost more than 80% of their initial energy. We comment that the proton temperature is of the order of 5 $\times 10^6$ °K, so that the proton thermal speed is $v_p \simeq 200$ km/s and the wave modes are subsequently suppressed because of proton Landau damping. This is consistent with the wave measurements shown in Figure 4. Following the time marked 3 (1234:27 UT) until 4 (1233:50 UT) the value of V_{px} continues to decrease to almost zero. However, the data are indicative of a different interaction. The slowing down is characterized by very weak electrostatic activity and, most important, by an increase in the value of V_{pz}, which reaches 250 km/s when V_{px} approaches zero. This is the type of interaction expected from Larmor coupling described by (1) and (2) for $v^* < \Omega_p$. It is basically a gyration of the protons about the magnetic field which is piled up in the front of the barium cloud. This stage is followed by entry into the magnetic cavity. We can associate the observed sunward flux of 0.5-keV protons with the thermal expansion of the protons when V_{px} became small.

The detailed spectrum presented in Figure 4 allows a further comparison with theoretical concepts. As noted before, the instability saturates by trapping. For the proton-barium situation and with $\alpha \ll 1$ the phase velocity V_{ph} of the unstable waves lies near the barium flow velocity (see Figure 6). In the solar wind reference frame we note that [Lampe et al., 1975]

$$V_{ph} = V_{px}(1 - 2^{-4/3}\alpha^{1/3}) \qquad (9)$$

Waves growing with this phase velocity will trap protons when their potential is of the order of

$$e\Phi = \tfrac{1}{2}\, m_p V_{ph}{}^2 \approx \tfrac{1}{2}\, m_p V_{px}{}^2 \qquad (10a)$$

and barium when

$$e\Phi = \tfrac{1}{2} m_b \left(\frac{\alpha}{2}\right)^{2/3} V_{px}{}^2 \tag{10b}$$

By comparing (10a) and (10b) we find that as long as

$$\frac{n_b}{n_p} > 2\left(\frac{m_p}{m_b}\right)^{1/2} \approx 0.17 \tag{11}$$

the condition for proton trapping (10a) will be reached first and will saturate the instability. Since in our case (11) is satisfied, we expect that the instability will saturate by trapping the protons. This is similar to the saturation of the Buneman instability studied by Davidson et al. [1970] which saturates by trapping electrons rather than protons, despite the fact that V_{ph} is near the proton beam. The amplitude of the electric field required to trap the protons is

$$\tilde{E} \approx \frac{1}{4} \frac{m_p V_{px}}{e} \omega_{Hp} \tag{12}$$

For the parameters given in Table 1 (i.e., $V_{px} = 250$–400 km/s and $\omega_{Hp} = 107$–145 s^{-1}) we find that (12) predicts $\tilde{E} = 67$–145 mV/m. Gurnett et al. [1985] report values of $\tilde{E} \approx 140$ mV/m while noting that the 10-Hz channel was saturated. Thus these field values are consistent with the saturation by trapping. Note that the peak spectral density in Figure 5 is $\lesssim 20$ Hz, which is consistent with theoretical values. The value of v^* can be estimated on the basis of the wave spectral energy density $S(\omega)$ in the lower hybrid region, as given in Figure 4. It is approximately given by [Papadopoulos, 1977]

$$v^* \approx \frac{D}{(V_{px} - V_{ph})^2} \approx \frac{e^2}{m_p{}^2} \frac{S(\omega \approx \omega_{Hp})}{V_{px}{}^2}$$

$$= 100 \left(\frac{100 \text{ km/s}}{V_{px}}\right)^2 \left(\frac{S(\omega \approx \omega_{Hp})}{10^{-4} \text{ V}^2/\text{m}^2 \text{ Hz}}\right)$$

where D is the diffusion coefficient in velocity space. For the measured values at 1234:27 and $S(\omega \approx \omega_{Hp})$ given by Figure 4 we find $v^* \approx 12$–20, so that $v^* \gg \Omega_p, \Omega_b$.

5. SUMMARY AND CONCLUSIONS

We have presented an analysis of previously reported observations on the solar wind–barium interaction associated with the AMPTE artificial comet release of December 27, 1984. On the basis of these results we have argued that the solar wind couples momentum (and energy) to the barium ions through both laminar and turbulent processes (see (1)). The laminar forces acting on the particles are the laminar electric and magnetic fields; the turbulent forces are associated with the intense electrostatic wave activity. This wave activity has been shown to be caused by a cross-field proton–barium ion streaming instability. The observed wave frequencies and saturated amplitudes are consistent with our theoretical analysis.

The following picture emerges. After the barium is released from the canisters, it expands outward and is photoionized. The expanding barium cloud forms a compressed density and magnetic field region on the sunward side of the expansion. As the solar wind protons stream into this region, they first interact with the barium ions to generate relatively weak off-angle electrostatic turbulence. This occurs when $n_b/n_p \lesssim 1$ and $V_{ap}/V_{px} \lesssim 1$. This turbulence acts to couple the solar wind protons and barium ions, and the protons slow down (see in

Figure 1 between marks 1 and 2). As the protons move deeper into barium ion shells, they encounter the compressed magnetic field region (which increases the local proton Alfvén speed) and a more dense barium ion region (which increases n_b/n_p). These two factors allow stronger wave growth to occur; this corresponds to the intense wave activity observed between the times marked 2 and 3 in Figure 3. This turbulence causes the solar wind protons to slow down even more and also produces proton and barium ion heating. Finally, the protons undergo a gyration about the compressed magnetic field which is indicated by a decrease in V_{px} and an increase in V_{pz}. We expect a similar type of interaction to occur in the solar wind–comet interaction. This topic is currently under study and will be reported elsewhere.

There are two more points that we would like to address. The first is about the electron heating and electron acceleration. The observed electron heating seems consistent with adiabatic heating. However, in addition to the local heating, the UK spacecraft observed electron fluxes with energy larger than 100 eV, i.e., the period between our marks 1 and 3. This is the period during which the lower hybrid instability was operating. For the flute mode ($k_y = 0$) instability discussed above, the electrons are adiabatic. However, field-aligned suprathermal electron tails can be produced by the nonflute modes ($k_y \neq 0$), corresponding to the electron-ion modes mentioned in section 3. These modes have frequencies typically $5f_{Hp}$–$6f_{Hp}$ and saturate at a lower level. The details of this interaction will be discussed elsewhere. It is sufficient here to note that the existence of wave frequencies in the 200-Hz to 1-kHz range is consistent with the model and with the electron fluxes observed by the UK spacecraft. Second, although the solar wind barium interaction results in complete momentum coupling, the barium has not been picked up by the solar wind during the 3–4 min of the measurements. This is due to the large barium mass and density which would require times of the order of 8–10 min to be picked up. This should be contrasted with the lithium releases for which pickup occurred at much shorter times.

REFERENCES

Davidson, R. C., N. A. Krall, K. Papadopoulos, and R. Shanny, Electron heating by electron-ion beam instabilities, Phys. Rev. Lett., 24, 579, 1970.

Fedder, J. A., J. G. Lyon, and J. L. Giuliani, Jr., Numerical simulations of comets: Predictions for comet Giacobini-Zinner, Eos Trans. AGU, 67, 17, 1986.

Gurnett, D. A., R. R. Anderson, B. Häusler, G. Haerendel, O. H. Bauer, R. A. Treumann, H. C. Koons, R. H. Holzworth, and H. Lühr, Plasma waves associated with the AMPTE artificial comet, Geophys. Res. Lett., 12, 851, 1985.

Haerendel, G., G. Paschmann, W. Baumjohann, and C. W. Carlson, Dynamics of the AMPTE artificial comet, Nature, 320, 720, 1986.

Ip, W.-H., and W. I. Axford, Theories of physical processes in the cometary comae and ion tails, in Comets, edited by L. L. Wilkening, University of Arizona Press, Tucson, 1982.

Lampe, M., W. M. Manheimer, and K. Papadopoulos, Anomalous transport coefficients for HANE applications due to plasma mi-

croinstabilities, *Memo. Rep. 3076*, Nav. Res. Lab., Washington, D. C., 1975.

McBride, J. G., E. Ott, J. P. Boris, and J. H. Orens, Theory and simulation of turbulent heating by the modified two-stream instability, *Phys. Fluids, 15*, 2367, 1972.

Mendis, D. A., and H. L. F. Houpis, The cometary atmosphere and its interaction with the solar wind, *Rev. Geophys., 20*, 885, 1982.

Papadopoulos, K., Review of anomalous resistivity for the ionosphere, *Rev. Geophys., 15*, 113, 1977.

Papadopoulos, K., R. Davidson, J. M. Dawson, I. Haber, D. A. Hammer, N. A. Krall, and R. Shanny, Heating of counterstreaming ion beams in an external magnetic field, *Phys. Fluids, 14*, 849, 1971.

Sagdeev, R. Z., V. D. Shapiro, and V. I. Shevchenko, MHD turbulence in the solar wind–comet interaction region, *Geophys. Res. Lett., 13*, 85, 1986.

Valenzuela, A., G. Haerendel, H. Föppl, F. Melzner, H. Neuss, E. Rieger, J. Stöcker, O. Bauer, H. Höfner, and J. Loidl, The AMPTE artificial comet experiments, *Nature, 320*, 700, 1986.

J. D. Huba, Naval Research Laboratory, Code 4780, 4555 Overlook Avenue, S.W., Washington, DC 20375.

A. T. Y. Lui, Applied Physics Laboratory, Johns Hopkins University, Laurel, MD 20707.

K. Papadopoulos, Science Applications International Corporation, 1710 Goodridge Drive, P. O. Box 1303, McLean, VA 22102.